Contents lists available at ScienceDirect

Journal of Materials Science & Technology

journal homepage: www.jmst.org

Effects of welding speed on the multiscale residual stresses in friction stir welded metal matrix composites

X.X. Zhang [a], L.H. Wu [a], H. Andrä [b], W.M. Gan [c], M. Hofmann [d], D. Wang [a], D.R. Ni [a], B.L. Xiao [a], Z.Y. Ma [a,*]

[a] *Shenyang National Laboratory for Materials Science, Institute of Metal Research, Chinese Academy of Sciences, Shenyang 110016, China*
[b] *Fraunhofer Institute for Industrial Mathematics, Fraunhofer-Platz 1, Kaiserslautern 67663, Germany*
[c] *German Engineering Materials Science Centre, Helmholtz-Zentrum Geesthacht, D-21502 Geesthacht, Germany*
[d] *Heinz Maier-Leibnitz Zentrum (MLZ), Technische Universität München, D-85747 Garching, Germany*

ARTICLE INFO

ABSTRACT

The effects of welding speed on the macroscopic and microscopic residual stresses (RSes) in friction stir welded 17 vol.% SiCp/2009Al-T4 composite plates were studied via neutron diffraction and an improved decoupled hierarchical multiscale modeling methods. Measurements showed that the macroscopic and total RSes had the largest variations in the longitudinal direction (LD). Increasing the welding speed led to higher values of measured LD macroscopic and total RSes in the matrix. The welding speed also significantly influenced the distributions and magnitudes of the microscopic RSes. The RSes were predicted via an improved hierarchical multiscale model, which includes a constant coefficient of friction based thermal model. The RSes in the composite plates before friction stir welding (FSW) were computed and then set as the initial states of the FSW process during modeling. This improved decoupled multiscale model provided improved predictions of the temperature and RSes compared with our previous model.

© 2019 Published by Elsevier Ltd on behalf of The editorial office of Journal of Materials Science & Technology.

1. Introduction

Metal matrix composites (MMCs) are broadly used in advanced applications owing to their excellent combined properties [1,2]. Friction stir welding (FSW) is considered to be a promising technique to join MMCs [3]. Significant residual stresses (RSes), particularly the microscopic ones, are known to inherently develop in MMCs during FSW due to the heterogeneous thermo-mechanical deformation [4], and they are heritable and variable during subsequent processes and service life [5]. The tensile RSes are detrimental to the structural integrity of MMCs and their structures [6–8]. Therefore, precise characterization of RSes is particularly important.

So far, many work has shown that the FSW RSes do not have the small magnitudes as researchers believed in the early stage of FSW research [9–11]. The RSes in FSW MMCs are more complex than those in FSW alloys. In MMCs, the RSes contain both the macroscopic and microscopic ones originating from the elastic mismatch, thermal and plastic misfit between matrix and rein-

forcement. Hence it is more difficult to characterize the RSes in FSW MMCs. Recently, the present authors established a new experimental method to determine the macroscopic and microscopic RSes in FSW joints of MMCs via neutron diffraction [4]. Especially, the effects of rotation rate on the total RSes were assessed [4].

The welding speed is another important FSW parameter, which significantly affects both the temperature and the mechanical properties of the FSW joints [12]. Nevertheless, the effects of welding speed on the macroscopic and especially the microscopic RSes in FSW MMCs have not been reported yet. In fact, from the mechanical point of view, the heterogeneous microscopic RSes in each phase is critical for local damage behaviors in MMCs, such as crack initiation, healing and growth [6,13]. Therefore, it is important to assess the effects of FSW parameters for optimizing the RSes in FSW MMCs.

In our previous work, an enhanced multiscale modeling method was developed to predict the multiscale RSes in FSW MMCs [14]. The model considered the effects of initial RSes and temperature history dependent constitutive laws. The model gave reasonably well predictions of the macroscopic RS and some components of the microscopic RSes. However, the accuracy of the model needs further improvement.

This work aims at assessing the effects of welding speed on the multiscale RSes in FSW MMCs. A 17 vol.% SiCp/2009Al-T4 com-

Table 1
Coordinates of ten macro-micro points.

Macro-micro point	Coordinates (mm)		
	T	L	N
P0	0	150	1.55
P1	2	150	1.55
P2	4	150	1.55
P3	6	150	1.55
P4	8	150	1.55
P5	10	150	1.55
P6	12	150	1.55
P7	22	150	1.55
P8	32	150	1.55
P9	42	150	1.55

posite was studied. The multiscale RSes in the MMC welds were determined via neutron diffraction measurements. An improved decoupled multiscale model was developed from our previous work [14] to predict the RSes under different welding speeds. Comparison between the predictions and the measurements helps us to verify and improve the multiscale model in the future. Such a combined experiment-modeling work provides the impetus for developing a reliable methodology towards optimization, from process to performances of FSW of MMCs.

2. Experimental

2.1. Material and FSW

3.1 mm thick 17 vol.% SiCp/2009Al-T4 composite plates were used in the present work. The 2009Al alloy had a nominal composition of Al-4.0Cu-1.4 Mg (wt%) and SiC particles had an average size of 7 μm. The composites were fabricated using the powder metallurgy technique and subsequently hot rolled into plates at 480 °C. The detailed fabrication and rolling processes have been described in a previous study [15]. The composite plates were heat treated to T4 condition: solution treated at 516 °C for 1 h, water quenched and naturally aged for 7 days.

Composite plates with a size of 300 mm × 75 mm × 3.1 mm were friction stir welded parallel to the rolling direction, at welding speeds of 50 mm/min and 100 mm/min with a rotation rate of 1000 rpm. A cermet tool with a shoulder 14 mm in diameter and a cylindrical pin 5 mm in diameter and 2.7 mm in length was adopted. These FSW MMC samples are named as V50 (for 50 mm/min) and V100 (for 100 mm/min), respectively. The temperature history was recorded by embedding a K-type thermocouple at the point P2 (see Table 1 and Fig. 1).

In our previous work [14], the composite plates with the size of 300 mm × 75 mm × 3.1 mm were friction stir welded at a welding speed of 150 mm/min, also having 1000 rpm rotation rate and using the same cermet tool. This sample was named as V150, of which the measured RSes reported in the Ref. [14] were adopted for comparison. More detailed information about FSW of the composites was presented in the previous investigations [15–20].

2.2. Neutron diffraction

Neutron diffraction at the diffractometer STRESS-SPEC of FRM II [21] was applied to measure the three principal strains, along the longitudinal (L), transverse (T) and normal (N) directions, across the welds at the middle thickness and the middle weld length (see Fig. 1). The Si monochromator was selected using symmetric (400) reflection yielding a wavelength of $\lambda = 1.7458$ Å for the neutron diffraction. This wavelength enabled simultaneous measurement of the 2009Al (311) and 6H SiC (116) reflections at scattering angles of $2\theta_{Al} \sim 91°$ and $2\theta_{SiC} \sim 83°$, respectively. The

gauge volumes for measuring the L, T and N components of residual strains of V50, V100 and V150 were 2 mm × 2 mm × 1 mm, 20 mm × 1 mm × 1 mm, and 1 mm × 20 mm × 1 mm, respectively. The gauge volume for measuring the macroscopic strain free reference parameters of V50, V100 and V150 comb samples was 10 mm × 1 mm × 1 mm.

According to our previous work [4], the procedure for determining the macroscopic and several microscopic RSes in MMC welds via neutron diffraction is summarized as follows:

$$\sigma_i^{\mathrm{pa, tM+pM}} = 3K^{\mathrm{pa}}\varepsilon_i^{\mathrm{pa, tM+pM}} = 3K^{\mathrm{pa}}\frac{d_0^{\mathrm{pa, M+eM}} - d_0^{\mathrm{pa, a}}}{d_0^{\mathrm{pa, a}}} \tag{1}$$

$$\sigma_i^{\mathrm{ma, tM+pM}} = \frac{V}{V-1}\sigma_i^{\mathrm{pa, tM+pM}} = \frac{3VK^{\mathrm{pa}}}{V-1}\frac{d_0^{\mathrm{pa, M+eM}} - d_0^{\mathrm{pa, a}}}{d_0^{\mathrm{pa, a}}} \tag{2}$$

$$\varepsilon_i^{\beta, \mathrm{M+eM}} = \frac{d_i^{\beta} - d_0^{\beta, \mathrm{M+eM}}}{d_0^{\beta, \mathrm{M+eM}}} = \frac{\sin\theta_0^{\beta, \mathrm{M+eM}}}{\sin\theta_i^{\beta}} - 1 \tag{3}$$

$$\sigma_i^{\mathrm{M}} = (1-V)\sigma_i^{\mathrm{ma, M+eM}} + V\sigma_i^{\mathrm{pa, M+eM}} \tag{4}$$

$$\sigma_i^{\beta, \mathrm{eM}} = \sigma_i^{\beta, \mathrm{M+eM}} - \sigma_i^{\mathrm{M}} \tag{5}$$

$$\sigma_i^{\beta, \mathrm{total}} = \sigma_i^{\mathrm{M}} + \sigma_i^{\beta, \mathrm{eM}} + \sigma_i^{\beta, \mathrm{tM+pM}} \tag{6}$$

where σ is the stress, ε the strain, V the volume fraction of the reinforcement, K the bulk modulus, d the lattice parameter, and θ the diffraction angle. The superscripts m and p denote the matrix and the particles, respectively; superscript tM+pM the thermal misfit plus plastic misfit; superscript M the macroscopic; superscript eM the elastic mismatch; superscript β each phase in MMC (β = ma or pa); superscript a the absolute unstrained reference. The subscript i denotes the stress or strain component, i = L, T or N.

3. Multiscale modeling

Our previous work showed that considering initial RSes and applying temperature history dependent constitutive laws improved the predictions of both macroscopic and microscopic RSes [14]. Based on the hierarchical multiscale modeling framework proposed in our previous works [14,22,23], a further improved decoupled multiscale model was formulated within this framework. Two developments were made in the present work:

1) The heat source model was changed. The presence of ceramic particles changes the friction behaviors of the MMCs compared to the unreinforced alloys [24,25]. In the present model, the heat generation based on a constant friction coefficient μ was integrated. In addition, according to the reported data [26], the pressure p between the FSW tool and the work-piece varied with FSW parameters, i.e. welding speed in this work. This will be mentioned in section 2.1.

2) The method of setting the initial RSes was changed. In this multiscale model, the initial RSes were taken into account in the elastic predictor of the return mapping algorithm (RMA). Differently, in the previous model, the initial RSes were added when returning the stress state to the finite element assembling. This will be mentioned in Section 2.2.

3.1. Governing equations

At the macroscale level, the equilibrium equations for heat flow and mechanics were solved with respect to the initial and boundary conditions corresponding to the quenching and FSW processes. The governing equation for heat flow reads as follows:

$$\rho_{\mathrm{M}}c_{\mathrm{M}}\dot{T}_{\mathrm{M}} - \nabla \cdot (k_{\mathrm{M}}\nabla T_{\mathrm{M}}) = q \tag{7}$$
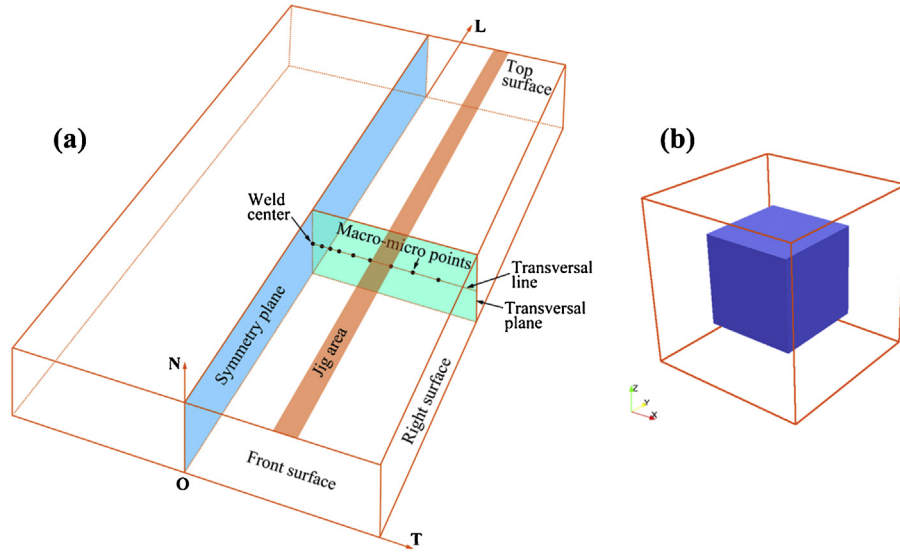
Fig. 1. Computational domains used in multiscale modeling [14]: (a) MMC plate, only the right half is modeled. Symmetry boundary conditions are imposed on the symmetry plane for macroscale modeling; (b) unit cell (UC) for microscale modeling.

where T denotes the temperature, β the density, c the heat capacity, k the heat conductivity, the upper dot denotes the time derivative.

A heat source model based on a constant friction coefficient was integrated. The heat generation rate q for the FSW process is computed as follows:

$$q = \mu p \left(\frac{2\pi\omega}{60} r + \frac{\upsilon}{60} \sin\varphi \right) \tag{8}$$

where ω is the rotation rate of FSW, r the distance away from the tool center, υ the welding speed of FSW, and ϕ the angle.

The previous work [26] has shown that the pressure p varies with changing the type of material and the welding parameters. For instance, for FSW of Al alloys, the pressure p increases with increasing the strength of the material or increasing the welding speed [26]. In the present work, the pressure p was set to 8.5 and 10.3 kN for V50 and V150, respectively.

With the definition of heat source from Eq. (8), the total heat generation Q can be calculated by summing up the shoulder heat generation Q_s and the pin heat generation Q_p:

$$Q = Q_s + Q_p \tag{9}$$

$$Q_s = \int_0^{2\pi} \int_{R_p}^{R_s} qr\,dr\,d\varphi \tag{10}$$

$$Q_p = \int_0^{2\pi} \int_0^{R_p} qr\,dr\,d\varphi + \int_0^{2\pi} \int_0^{h_p} qR_p\,dz\,d\varphi \tag{11}$$

where R_s and R_p are shoulder and pin radius, respectively, h_p the pin length.

The heat input W is defined by dividing the total heat generation by the welding speed:

$$W = \frac{Q}{\upsilon/60} \tag{12}$$

The quasi-static mechanical equilibrium equation within the infinitesimal deformation framework at the macroscale reads as follows:

$$\nabla \cdot \boldsymbol{\sigma}_M = 0 \tag{13}$$

where $\boldsymbol{\sigma}$ is the stress tensor.

At macroscale, the elastic law is as follows:

$$\boldsymbol{\sigma}_M = \boldsymbol{E}_{eff}\boldsymbol{\varepsilon}_M^e + \boldsymbol{\sigma}_M^{inital} \tag{14}$$

where $\boldsymbol{E}_{eff}$ is the effective elastic stiffness tensor [22], $\boldsymbol{\varepsilon}_M^e$ the elastic strain tensor, $\boldsymbol{\sigma}_M^{inital}$ the initial macroscopic residual stress.

Meanwhile, at macroscale, the MMC was assumed as a continuum media and was modeled by a J_2-flow theory of infinitesimal thermo-elastoplasticity [14,23], based on the effective properties determined by computational homogenization method [22]. The macroscopic yield function reads as follows:

$$f_M\left(\boldsymbol{\sigma}_M, \alpha_M, T, \dot{T}\right) = \sqrt{3/2}\,\big|\big|\text{dev}\left[\boldsymbol{\sigma}_M\left(\alpha_M, T, \dot{T}\right)\right]\big|\big|$$
$$- \sigma_M\left(\alpha_M, T, \dot{T}\right) \tag{15}$$

where $\boldsymbol{\sigma}$ is the stress tensor, α indicates the accumulated plastic strain, $||\bullet||$ denotes the norm of the indicated tensor, dev($\bullet$) the deviator of the indicated tensor, the isotropic hardening function $\sigma_M\left(\alpha_M, T, \dot{T}\right)$ is fitted utilizing spline interpolation function based on the effective properties determined by computational homogenization method [22].

At the microscale, the temperature was assumed homogeneous in each volume element corresponding to the macroscale integration point. This means:

$$T_{mi} = T_M^g \tag{16}$$

where subscript mi denotes the microscale and superscript g denotes the macroscale Gaussian integration point.

The quasi-static mechanical equilibrium equation within the infinitesimal deformation framework at the microscale reads as follows:

$$\nabla \cdot \boldsymbol{\sigma}_{mi} = 0 \tag{17}$$

At microscale, the elastic law was similar to that at macroscale, which is as follows:

$$\boldsymbol{\sigma}_{mi} = \boldsymbol{E}_{mi}\boldsymbol{\varepsilon}_{mi}^e + \boldsymbol{\sigma}_{mi}^{inital} \tag{18}$$

where $\boldsymbol{E}_{mi}$ is the elastic stiffness tensor, $\boldsymbol{\varepsilon}_{mi}^e$ the elastic strain tensor, and $\boldsymbol{\sigma}_{mi}^{inital}$ the initial microscopic residual stress.

At microscale, each phase in MMC was modeled by a J_2-flow theory of infinitesimal thermo-elastoplasticity [14,23]. For rigid ceramic reinforcements that normally undergo only elastic deformation, the corresponding yield stress was then simply set to a sufficient large value. The general yield condition at the microscale
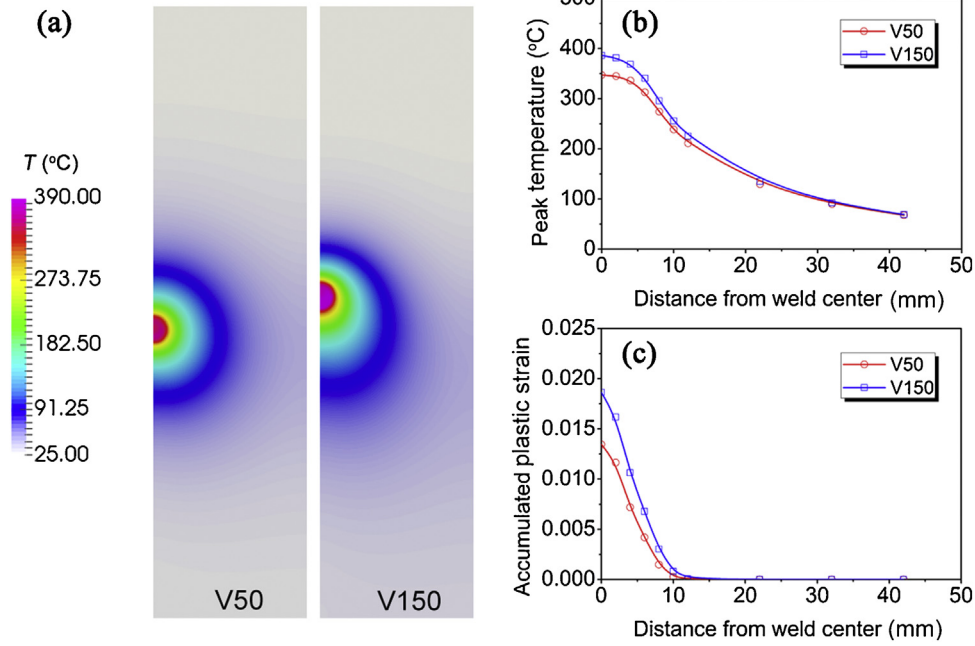
Fig. 2. Effects of welding speed on temperature fields (a), peak temperature (b) and accumulated plastic strain along the 'transversal line' defined in Fig. 1(a) (c).

reads as follows:

$$f_{mi}\left(\boldsymbol{\sigma}_{mi}, \alpha_{mi}, T, \dot{T}\right) = \sqrt{3/2}\left|\left|\mathrm{dev}\left[\boldsymbol{\sigma}_{mi}\left(\alpha_{mi}, T, \dot{T}\right)\right]\right|\right|$$
$$-\sigma_{mi}\left(\alpha_{mi}, T, \dot{T}\right) \qquad (19)$$

The Voce type isotropic hardening rule reads [27]

$$\sigma_{mi}\left(\alpha_{mi}, T, \dot{T}\right) = \sigma_{mi}^{\infty}\left(T, \dot{T}\right) + h_{mi}\alpha_{mi}$$
$$+ \left[\sigma_{mi}^0\left(T, \dot{T}\right) - \sigma_{mi}^{\infty}\left(T, \dot{T}\right)\right]\exp\left(l_{mi}\alpha_{mi}\right) \qquad (20)$$

where σ^0 is the initial yield strength, σ^{∞} the ultimate strength, both h and l are the material constants.

In this decoupled multiscale model, the boundary conditions for the microscale models are constructued using the macroscopic strains. To compute the macroscopic and elastic mismatch residual stresses, the kinematic uniform boundary conditions (KUBCs) of the microscale model I are constructed by [28]

$$\boldsymbol{u}_{mi}^{I} = \boldsymbol{\varepsilon}_{M}^{ep} \cdot \boldsymbol{x}_{mi} \qquad (21)$$

The thermal misfit plus plastic misfit RSes $\sigma_i^{\beta,\ tM+pM}$ can be computed by constructing the KUBCs for the microscale model II via the macroscale thermal strain $\boldsymbol{\varepsilon}_{M}^{th}$ [28]:

$$\boldsymbol{u}_{mi}^{II} = \boldsymbol{\varepsilon}_{M}^{th} \cdot \boldsymbol{x}_{mi} \qquad (22)$$

There is no need to calculate the homogenized stress tensor and modulus matrix from the microscale model for assembling the macrscopic model. The stress tensor and modulus matrix for assembling the macroscopic model are calculated using the macroscopic constitutive law based on Eqs. (14) and (15). Therefore, this model is called as a decoupled multiscale model.

3.2. Numerical solution scheme

The hierarchical coupling method was adopted to solve the multiscale problem, where the macroscale model was solved independently of the microscale models. The residual vector and the tangent stiffness matrix for all the macroscale integration points

were computed through the pre-determined macroscale constitutive model. In this work, 10 macro-micro points, where the microscale models were defined, were used. These points are listed in Table 1 and illustrated in Fig. 1(a).

In the present work, the well-known RMA for computational plasticity was applied at both the macroscale and microscale to update the stress states, which corresponds to the given strains at each time increment [29,30]. During the elastic predictor stage of the RMA, the initial RSes were taken into account in the present multiscale model.

After updating the stress state, for those integration points at the macroscale that were not macro-micro points, the tangent matrices for assembling the global equation at the macroscale were directly computed in the RMA. For the macro-micro points, the tangent matrices were determined via the six load cases method [31]. At the microscale, the tangent matrices for assembling the global equation at every integration points were computed in the RMA directly.

The computational domains at both the macroscale and microscale were discretized into unstructured tetrahedrons with 4-nodes by TetGen [32]. Linear shape functions were applied at both scales. The multiscale modeling was carried out with the software MSFESL developed by the present authors [14,22,23,28]. The temperature and multiscale RSes for V50 and V150 were modeled.

4. Results and discussion

4.1. Temperature

Fig. 2(a) shows the top view of the temperature fields of V50 and V150. It can be seen that in front of the welding tool the temperature gradient of V150 is larger than that of V50. Behind the welding tool, it is reversed. The peak temperatures at different locations (macro-micro points) away from the weld center of V150 are higher than those of V50 (Fig. 2(b)). The temperature gradients cause plastic deformation [6]. The higher the temperature gradient is, the larger degree of plastic strain is. The temperature gradient of V150 is higher than that of V50, so larger plastic strain occurs in V150 than that in V50 (Fig. 2(c)).
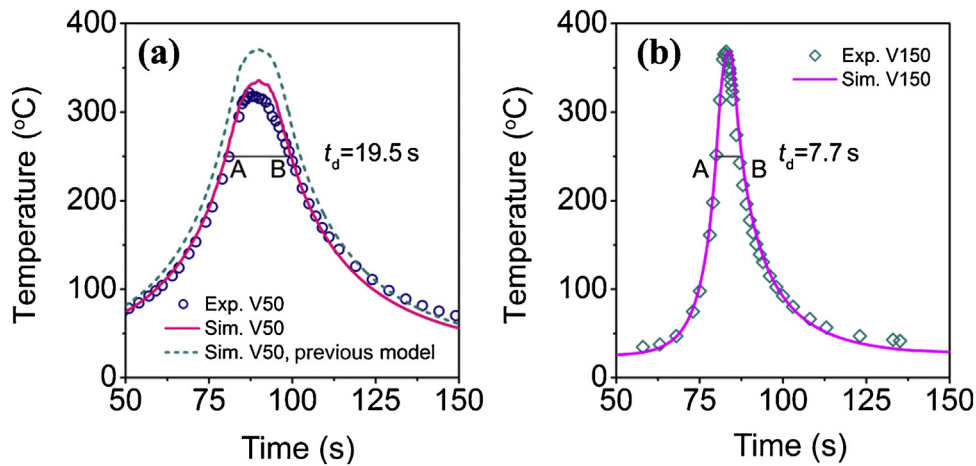
Fig. 3. Measured and predicted thermal cycles at location P2 for V50 (a) and V150 (b). The previous model in (a) means the multiscale model in the Ref. [14]. The line $\overline{AB}$ denotes the preservation time t_d when the temperature is above 250 °C. The measured temperature of V150 in.(b) is from our previous work [14].
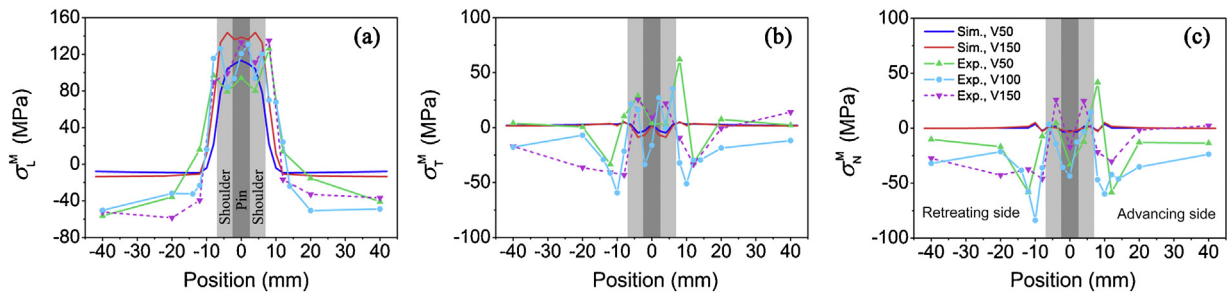

Fig. 4. Profiles of L (a), T (b) and N (c) macroscopic RSes cross welds at middle thickness and middle weld length for V50, V100 and V150. The experimental results of V150 are from our previous work [14].

The measured temperature data in Fig. 3(a) and (b) show that the peak temperature increased from 320 to 370 °C with increasing the welding speed from 50 to 150 mm/min, while the widths of the measured thermal cycle profiles reduced. Fig. 3 also compares the measured and predicted thermal cycles at position P2 (Table 1 and Fig. 1(a)). For both welding speeds, the predicted thermal cycles by the present model agree with the measured results very well. It reveals that a constant friction coefficient based thermal model with a varied pressure is verified. In our previous work where the thermal model was based on a temperature dependent friction coefficient [14], the predicted thermal cycle was also in agreement with the measured data for V150. However, the peak temperature of the predicted thermal cycle using previous multiscale model is about 50 °C higher than the experimental result for V50 [14]. Therefore, it can be seen that for modeling the temperature fields of FSW MMCs, a constant friction coefficient based thermal model with a varied pressure is better.

4.2. Macroscopic RS

Typically, the welding processes generate macroscopic RSes that have their largest total variation in the L direction. The L macroscopic RS is characterized by tension from the weld center to the heat affected zone (HAZ) and compression in the base material. The maximum *L* tensile macroscopic RS usually appears near the shoulder edge for FSW [10]. In this study, the measured macroscopic RSes showed similar behaviors, as shown in Fig. 4. For some cases, the profile of the L macroscopic RS is an "inverted-V" shaped with the maximum value located near the weld center [10]. Such cases are related to the special evolution histories of microstruc-
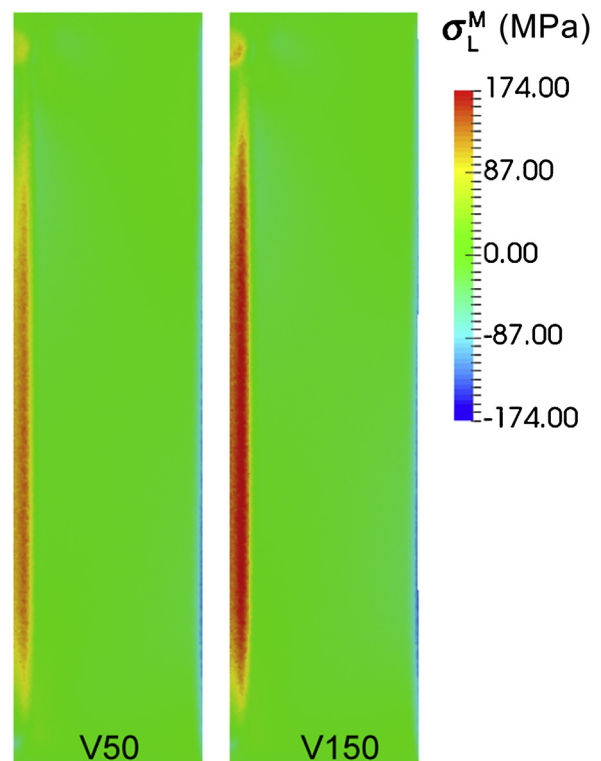

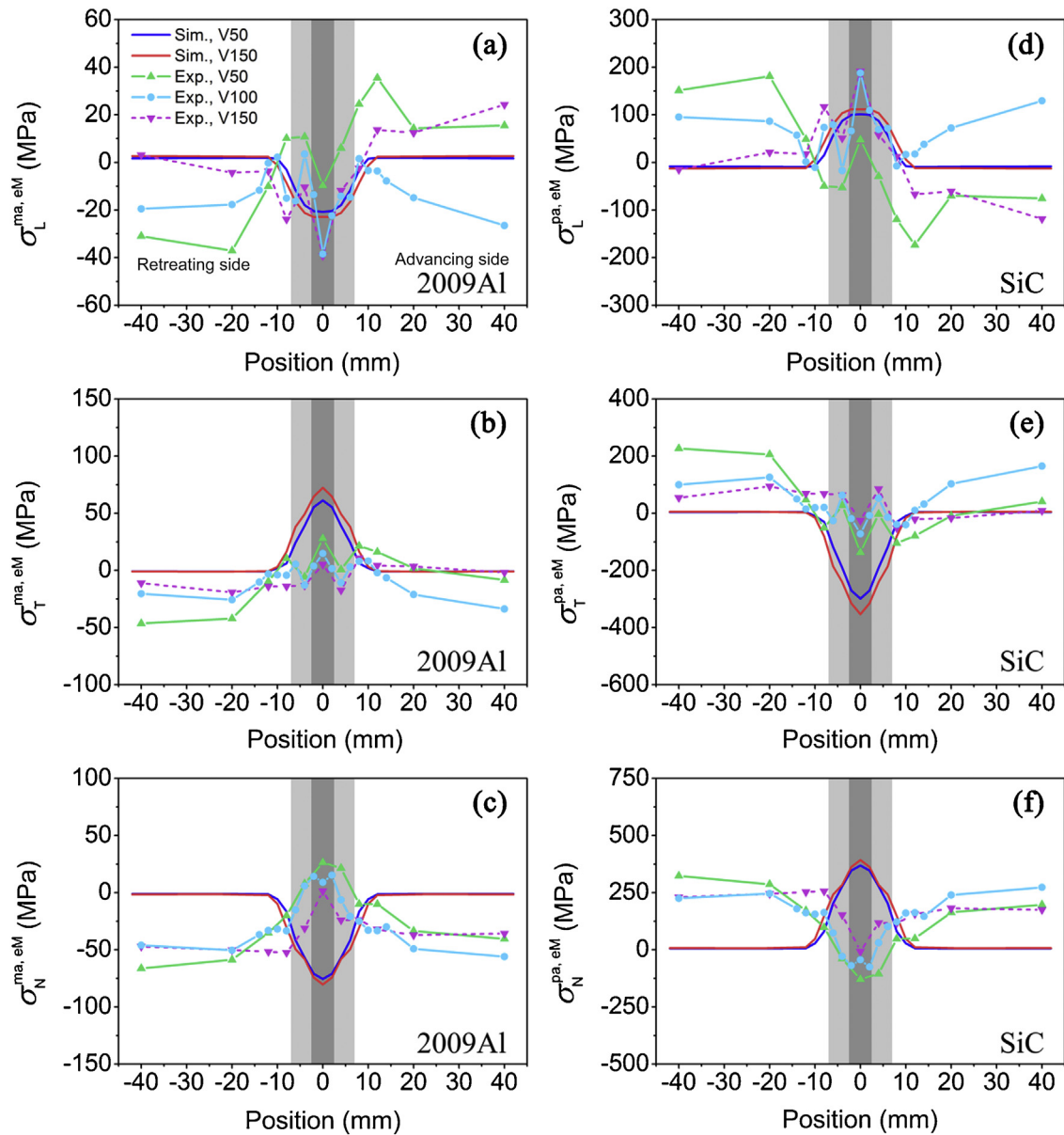**Fig. 5.** Effects of welding speed on L macroscopic RS fields.

Fig. 6. Profiles of L, T and N elastic mismatch RSes cross welds at middle thickness and middle weld length for V50, V100 and V150: (a) L, (c) T and (e) N components in 2009Al matrix; (b) L, (d) T and (f) N components in reinforcement. The experimental results of V150 are from our previous work [14].

tures and plastic properties (especially the yield strength and the strain hardening rate) in the joints.

Lower welding speed or higher rotation rate results in a broader profile of the tensile zone of the L macroscopic RS due to the higher heat input [33]. For instance, Lombard et al. [34] found that the width of the tensile RS zone was proportional to the heat input in the FSW 5083Al-H321 plates, while the maximum value of the tensile RS is inversely proportional to the heat input. Furthermore, the maximum tensile macroscopic RS is not directly proportional to the maximum temperature [33]. In this study, the welding speed increased from 50 to 150 mm/min, i.e. increased by three times. According to Eqs. (8)–(11), the total heat generation Q increased from V50 to V150, as indicated by the temperature in Fig. 2(b). However, Q did not increase three times according to Eq. (8). Therefore, the heat input W decreased with increasing the welding speed from 50 to 150 mm/min according to Eq. (12). This phenomenon was also been observed in a previous study [35].

Fig. 4(a) shows that the measured L macroscopic RS σ_L^M within the shoulder edge increased. Meanwhile, the peak values of σ_L^M for

V150, V100 and V50 were ∼135, ∼131 and ∼126 MPa, respectively. This trend agrees with previous results.

Fig. 4(b) and (c) shows that the measured T and N macroscopic RSes (σ_T^M and σ_N^M) have significant magnitudes, with a variation of ∼100 MPa in the amplitude. During the FSW process, the rigid clamps exert much higher constraints on the deformation of the welded plates. These constraints hinder the contraction along the L and T directions of the stir zone (from about -12 mm position to about 12 mm position in Fig. 4) due to cooling, causing significant L and T macroscopic RSes [34,36–38]. A higher welding speed decreases the width of the profiles of the measured stresses σ_T^M and σ_N^M (Fig. 4(b) and (c)).

Fig. 4 shows that the predictions can reproduce the basic profiles of σ_i^M. Notice that symmetrical macroscopic model was assumed as shown in Fig. 1. Therefore, the predicted RSes are symmetrical with respective to the butting face, e.g. 0 position in Fig. 4. The predictions also reproduce the effects of welding speed on the magnitude of σ_i^M, see Fig. 4(a). However, in the predictions lower welding speed has narrower width of tensile L macroscopic RS zone, which
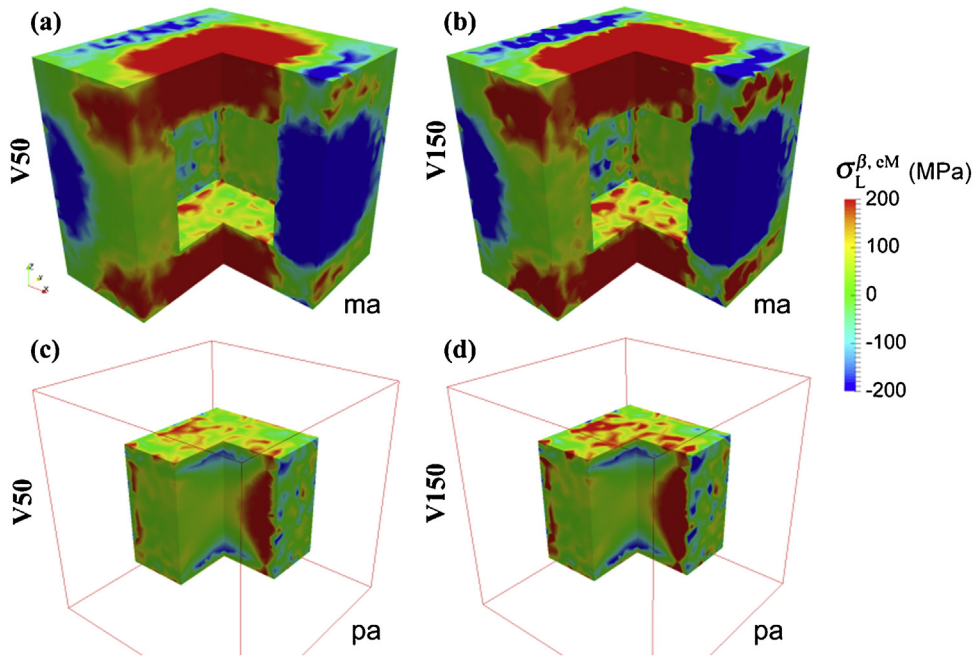
Fig. 7. Longitudinal elastic mismatch RS fields of matrix and reinforcement at macro-micro point P0 for V50 (a, c) and V150 (b, d).

differs from the measurements. In addition, significant errors exist in σ_T^M and σ_N^M between the predictions and measurements.

Fig. 5 shows the maps of the L macroscopic RSes of V50 and V150. It can be seen that both the magnitude and the area (especially the length along the L direction) of the L macroscopic RS with high tensile values for V150, i.e. the red region, exceed those for V50.

4.3. Elastic mismatch RS

Fig. 6 shows that the total variations of the measured elastic mismatch RSes in the matrix $\sigma_i^{ma, eM}$ decrease at a higher welding speed. The profile of the measured $\sigma_L^{ma, eM}$ of V50 is significantly asymmetrical, which is probably due to the variations of microstructure, mechanical properties and initial RS state between the two MMC plates before FSW. In addition, increasing the welding speed moves $\sigma_i^{ma, eM}$ towards compression and decreased the width of the profiles of $\sigma_i^{ma, eM}$ with high magnitude. The profiles of $\sigma_i^{pa, eM}$ are opposite to those of $\sigma_i^{ma, eM}$, while the ratio of their total variations obeyed (100%-17%): 17%, i.e. about 4.9 : 1.0. The experimental results reveal that increasing the welding speed tends to reduce the load transfer from the matrix to the particles. This trend is partially caused by the variation of the macroscopic RS and is partially due to the change in the microstructures of the welds [4].

Fig. 7 shows the L elastic mismatch RS maps of the matrix and the reinforcement at the maco-micro point P0. The maps are very close to each other for V50 and V150. It can be seen that the variation trends in the predictions are smaller than those in the measurements.

4.4. Thermal misfit plus plastic misfit RS

Fig. 8(a) shows that in the BM the measured thermal misfit plus plastic misfit RS in the matrix $\sigma^{ma, tM+pM}$ of V50, V100 and V150 had the same level, with a value of ∼80 MPa. In the stir zone the measured thermal misfit plus plastic misfit RS in the matrix $\sigma^{ma, tM+pM}$ raises with increasing the welding speed. This differs from the change of the rotation rate. Our previous work showed that increasing the rotation rate from 600 to 1500 rpm, $\sigma^{ma, tM+pM}$ approximately kept its level in both the BM and the stir zone [4].

The welding speed of V50 is 1/3 of V150, therefore, as shown in Fig. 3, the preservation time (e.g. above 250 °C) for coarsening and dissolution of precipitates in the stir zone and the heat affected zone of V50 is approximate three times of those of V150. As a result, the strength of the joint of V50 should be lower than that of V150, such phenomenon was confirmed by many previous investigations about FSW of Al alloys and SiC/Al composites [12,20,39,40]. For example, Wang et al. [20] showed that higher welding speed resulted in higher strength of the FSW joints of SiCp/2009Al-T4 composite. As a result, larger plastic deformation occurred in the 2009Al matrix during cooling of V50 due to the lower yield strength compared with that in V150.

Larger plastic deformation causes more release of thermal misfit plus plastic misfit RS. Hence, the measured $\sigma^{ma, tM+pM}$ in the stir zone and the HAZ of V50 is lower than that of V150, as shown in Fig. 8(a). As expected, Fig. 8(b) shows that the profiles of $\sigma_i^{pa, tM+pM}$ are opposite to those of $\sigma_i^{ma, tM+pM}$, while the ratio of their total variations obeyed about 4.9 : 1.0.

Fig. 8 shows that the predicted thermal misfit plus plastic misfit RSes $\sigma_i^{\beta, tM+pM}$ from the present multiscale model agrees with those measured data. Especially, the predicted thermal misfit plus plastic misfit RS in the matrix $\sigma_i^{ma, tM+pM}$ in the stir zone is lower than that in the BM, which agrees with the present and our previous experimental results [4]. In contract, using the previous multiscale model [14], the predicted $\sigma_i^{ma, tM+pM}$ in the stir zone is much higher than (about twice of) that in the base material (BM). Therefore, it can be seen that the present multiscale model is more accurate than the previous one [14].

Fig. 9 shows the L thermal misfit plus plastic misfit RS maps of the matrix and the reinforcement at the maco-micro point P0 for V50 are similar with those for V150. In the present multiscale model, the effect of thermal cycle on the plastic properties including the yield strength and plastic hardening parameters was approximately modeled by a temperature history dependent hardening law (see Eqs. (15) and (19)). Such an approximation is probably the reason for the rough estimation of thermal misfit plus plastic misfit RS. Further improvement requires a more accurate material constitutive law.
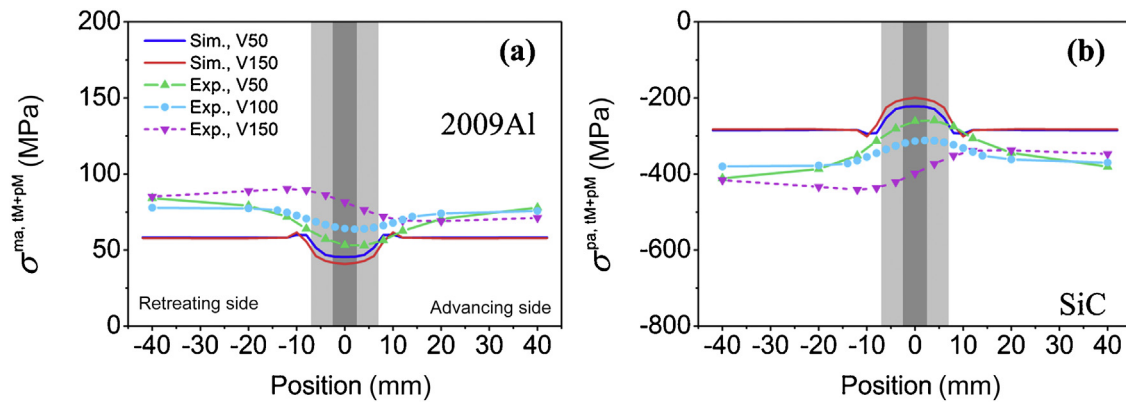
Fig. 8. Comparison of profiles of thermal misfit residual stress cross welds at middle thickness and middle weld length for V50, V100 and V150: (a) in 2009Al matrix; (b) in reinforcement. The experimental results of V150 are from our previous work [14].
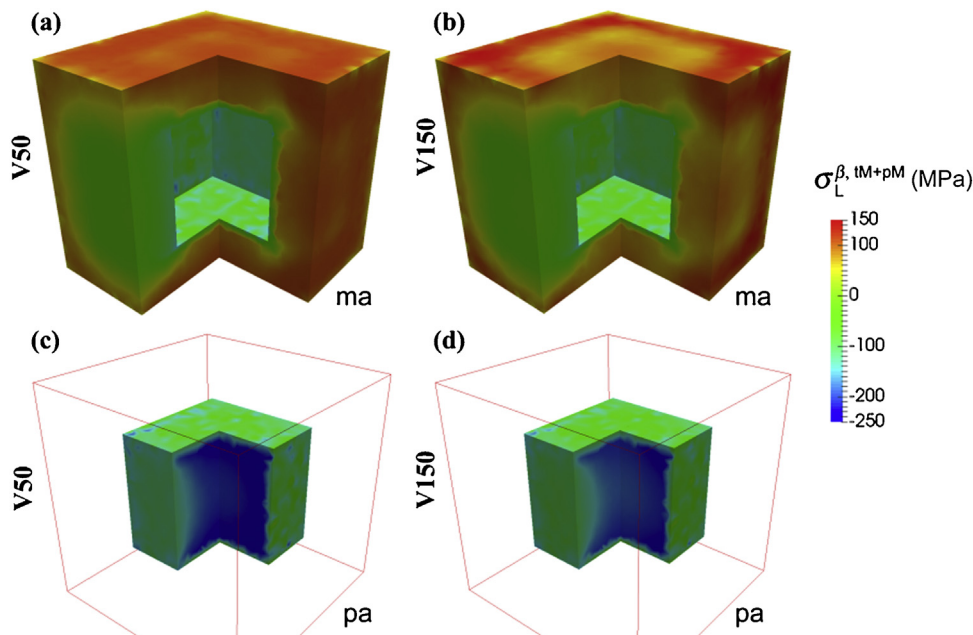

Fig. 9. Longitudinal thermal plus plastic misfit RS fields of matrix and reinforcement at macro-micro point P0 for V50 (a, c) and V150 (b, d).

4.5. Remarks on the multiscale modeling of residual stress

So far, accurate prediction of the residual stresses (especially the microscopic ones) is still difficult because they are heritable and variable during every processing stage in manufacturing [6]. In the present case, before FSW, initial RSes including macroscopic and microscopic ones already existed in the rolled 17 vol.% SiCp/2009Al-T4 composite plates, which were mainly induced by the rolling and quenching processes. These RSes can be determined either via multiscale modeling or measurements. In our previous and the present studies, these initial RSes were modeled based on the assumption, in which the initial RSes were only induced by the quenching process. However, the multiscale model to predict the initial multiscale RSes probably missed some facts, e.g. the rolling process.

Our previous study showed that the solution treatment and quenching process could not eliminate the pre-exist RSes [14]. Therefore, the initial RSes in the composite plates were a product of all the processing stages before FSW. In this regard, measurements via neutron or synchrotron X-ray diffraction are preferred to obtain the initial RS states for accurate predictions of the FSW process. In addition, the effect of texture generated during the rolling process was not considered. Texture causes anisotropic mechanical behavior [41,42], while in the present work both the macroscale and the microscale models were assumed isotropic.

Concerning the microscopic RSes, application of real microstructure based representative volume element will improve the accuracy of predictions, with increasing the computational cost [23]. Another way to obtain more accurate predictions of the microscopic RSes is to apply the periodic boundary conditions (PBCs) rather than the KUBCs [23]. However, it is convenient to apply the PBCs with structural mesh, while applying PBCs with unstructured tetrahedron mesh is difficult.

5. Conclusions

The present work studied the influences of welding speed on the multiscale RSes in FSW 17 vol.% SiCp/2009Al composites using neutron diffraction and a decoupled hierarchical multiscale modeling methods. The following conclusions can be summarized:

(1) Increasing the welding speed increases the magnitudes of the measured L macroscopic RS σ_L^M within the shoulder edge, and decreases the widths of σ_T^M and σ_N^M with high magnitudes. The

peak values of σ_L^M for V50, V100 and V150 were $\sim$126, $\sim$131 and $\sim$135 MPa, respectively. Significant T and N macroscopic RSes are measured, which have significant magnitudes, with a variation of $\sim$100 MPa in the amplitude.

(2) Increasing the welding speed decreases the total variations of the measured elastic mismatch RSes in the matrix $\sigma_i^{ma,\ eM}$, and moves $\sigma_i^{ma,\ eM}$ towards compression and decreases the width of their profiles with high magnitude. In the stir zone the measured thermal misfit plus plastic misfit RS in the matrix $\sigma^{ma,\ tM+pM}$ raises with increasing the welding speed. The profiles of $\sigma_i^{pa,\ eM}$ and $\sigma^{pa,\ tM+pM}$ are opposite to those of $\sigma_i^{ma,\ eM}$ and $\sigma^{ma,\ tM+pM}$, respectively, while the ratio of their total variations obeys about 4.9 : 1.0.

(3) The new multiscale model provides better predictions, especially the temperature and the thermal misfit plus plastic misfit RS, compared with the previous multiscale model [14]. Some basic influences of welding speed on different components of the macrosocpic RS, the L and T components of the elastic mismatch are reproduced by the predictions. In the present multiscale, the predicted thermal misfit plus plastic misfit RSes agrees the measured ones reasonably well.

Acknowledgments

References

[1] D.B. Miracle, Compos. Sci. Technol. 65 (2005) 2526–2540.
[2] L.J. Huang, L. Geng, H.X. Peng, Prog. Mater. Sci. 71 (2015) 93–168.
[3] D. Wang, B.L. Xiao, D.R. Ni, Z.Y. Ma, Acta Metall. Sin. (Engl. Lett.) 27 (2014) 816–824.
[4] X.X. Zhang, D.R. Ni, B.L. Xiao, H. Andrae, W.M. Gan, M. Hofmann, Z.Y. Ma, Acta Mater. 87 (2015) 161–173.
[5] W.C. Jiang, W. Woo, G.B. An, J.U. Park, Mater. Des. 51 (2013) 415–420.
[6] P.J. Withers, Rep. Prog. Phys. 70 (2007) 2211–2264.
[7] M.N. Ilman, M.R. Kusmono, N. Muslih, H. Subeki, Wibowo, Mater. Des. 99 (2016) 273–283.
[8] D.P. Wang, H. Zhang, B.M. Gong, C.Y. Deng, Mater. Des. 91 (2016) 211–217.
[9] W. Woo, H. Choo, M.B. Prime, Z. Feng, B. Clausen, Acta Mater. 56 (2008) 1701–1711.
[10] W. Woo, Z. Feng, X.L. Wang, S.A. David, Sci. Technol. Weld. Join. 16 (2011) 23–32.
[11] H.J. Aval, Mater. Des. 87 (2015) 405–413.
[12] Z.Y. Ma, A.H. Feng, D.L. Chen, J. Shen, Crit. Rev. Solid State Mater. Sci. 43 (2018) 269–333.
[13] M. Schoebel, G. Baumgartner, S. Gerth, J. Bernardi, M. Hofmann, Acta Mater. 81 (2014) 401–408.
[14] X.X. Zhang, D. Wang, B.L. Xiao, H. Andrae, W.M. Gan, M. Hofmann, Z.Y. Ma, Mater. Des. 115 (2017) 364–378.
[15] D.R. Ni, D.L. Chen, B.L. Xiao, D. Wang, Z.Y. Ma, Int. J. Fatigue 55 (2013) 64–73.
[16] D.R. Ni, D.L. Chen, D. Wang, B.L. Xiao, Z.Y. Ma, Mater. Des. 51 (2013) 199–205.
[17] D.R. Ni, D.L. Chen, D. Wang, B.L. Xiao, Z.Y. Ma, Mater. Sci. Eng. A 608 (2014) 1–10.
[18] D. Wang, B.L. Xiao, Q.Z. Wang, Z.Y. Ma, Mater. Des. 47 (2013) 243–247.
[19] D. Wang, B.L. Xiao, Q.Z. Wang, Z.Y. Ma, J. Mater. Sci. Technol. 30 (2014) 54–60.
[20] D. Wang, Q.Z. Wang, B.L. Xiao, Z.Y. Ma, Mater. Sci. Eng. A 589 (2014) 271–274.
[21] M. Hofmann, R. Schneider, G.A. Seidl, J. Rebelo-Kornmeier, R.C. Wimpory, U. Garbe, H.G. Brokmeier, Phys. B 385–386 (2006) 1035–1037.
[22] X.X. Zhang, B.L. Xiao, H. Andrae, Z.Y. Ma, Compos. Struct. 113 (2014) 459–468.
[23] X.X. Zhang, B.L. Xiao, H. Andra, Z.Y. Ma, Compos. Struct. 137 (2016) 18–32.
[24] A. Martin, J. Rodriguez, J. Llorca, Wear 225 (1999) 615–620.
[25] T.W. Scharf, P.G. Kotula, S.V. Prasad, Acta Mater. 58 (2010) 4100–4109.
[26] M.J. Peel, A. Steuwer, P.J. Withers, T. Dickerson, Q. Shi, H. Shercliff, Metall. Mater. Trans. A 37 (2006) 2183–2193.
[27] E. Voce, Metallurgica 51 (1955) 219–226.
[28] X.X. Zhang, B.L. Xiao, H. Andra, Z.Y. Ma, Compos. Struct. 125 (2015) 176–187.
[29] J.C. Simo, T.J.R. Hughes, Computational Inelasticity, Springer-Verlag, New York, 1998.
[30] E.A. de Souza Neto, D. Perić, D.R.J. Owen, Computational Methods for Plasticity: Theory and Applications, John Wiley & Sons Ltd, West Sussex, 2008.
[31] T.I. Zohdi, P. Wriggers, An Introduction to Computational Micromechanics, Corrected Second Printing, Springer, Berlin-Heidelberg, 2005.
[32] H. Si, TetGen: A Quality Tetrahedral Mesh Generator and Three-dimensional Delaunay Triangulator, 2018, September 24 http://wias-berlin.de/software/index.jsp?id=TetGen&lang=1.
[33] C.C. Tutum, J.H. Hattel, Sci. Technol. Weld. Join. 15 (2010) 369–377.
[34] H. Lombard, D.G. Hattingh, A. Steuwer, M.N. James, Mater. Sci. Eng. A 501 (2009) 119–124.
[35] X.X. Zhang, B.L. Xiao, Z.Y. Ma, Metall. Mater. Trans. A 42 (2011) 3229–3239.
[36] M. Peel, A. Steuwer, M. Preuss, P.J. Withers, Acta Mater. 51 (2003) 4791–4801.
[37] V.M. Linton, M.I. Ripley, Acta Mater. 56 (2008) 4319–4327.
[38] M.Z.H. Khandkar, J.A. Khan, A.P. Reynolds, M.A. Sutton, J. Mater. Process. Technol. 174 (2006) 195–203.
[39] A.H. Feng, D.L. Chen, Z.Y. Ma, W.Y. Ma, R.J. Song, Acta Metall. Sin. (Engl. Lett.) 27 (2014) 723–729.
[40] Z. Zhang, B.L. Xiao, Z.Y. Ma, Acta Mater. 73 (2014) 227–239.
[41] E. Salvati, A.M. Korsunsky, Int. J. Plast. 98 (2017) 123–138.
[42] E. Maawad, W. Gan, M. Hofmann, V. Ventzke, S. Riekehr, H.G. Brokmeier, N. Kashaev, M. Mueller, Mater. Des. 101 (2016) 137–145.